Brazilian Journal of Geophysics 43 (2025), 2, 1-28
Brazilian Geophysical Society
ISSN 2764-8044
DOI: 10.22564/brjg.v43i2.2338

Crustal Accretion, Significant Mantle Uplift, and Exhumation along Non-transform Discontinuities: Equatorial Mid-Atlantic Ridge (7º 10' – 0º 50' N)

Heliásio Augusto Simões[1], Moab Praxedes Gomes[2]*, Patrícia Reis Alencar Oliveira[1], Mauro Lisboa Souza[1], Hugo Leonardo de Andrade Rocha[3], and Vadim Harlamov[3]

[1]Serviço Geológico do Brasil – SGB, Fortaleza, CE, Brazil
[2]Universidade do Rio Grande do Norte – UFRN, Natal, RN, Brazil
[3]Serviço Geológico do Brasil – SGB, Rio de Janeiro, RJ, Brazil

Simões, H. A.: https://orcid.org/0000-0001-6587-6386
Gomes, M. P.: https://orcid.org/0000-0003-0836-1073
Oliveira, P. R. A.: https://orcid.org/0000-0001-9647-7994
Souza, M. L.: https://orcid.org/0000-0002-3425-9622
Rocha, H. L. A.: https://orcid.org/0000-0001-7911-2192
Harlamov, V.: https://orcid.org/0000-0002-5971-920X

*Corresponding author email: moab.gomes@ufrn.br

ABSTRACT. The exhumation and exposure of mantle rocks is a common process that takes place during the tectono-magmatic evolution of a newly created lithosphere along slow- and ultraslow-spreading oceanic ridges, such as the Equatorial Mid-Atlantic Ridge. A geophysical survey conducted in 2012 and 2013 between the Bogdanov (7º 10' N) to the St. Paul (0º 50' N) fracture zones revealed lower crust and upper mantle rocks exposures through asymmetric accretion along low-angle normal faults, i.e., the Oceanic Core Complexes, laterally associated with other morpho-tectonic features. The dataset consists of multi-beam bathymetry (100 m/pixel) and ship gravity (1,750 m/pixel) covering an area of 40,000 km^2. Seismicity and satellite free-air anomaly data are included. Three oceanic transform faults and nine non-transform offsets were identified and mapped along the ridge axis. Oceanic Core Complexes are characterized by corrugated and non-corrugated massifs, back-tilted ridges indicating detachment breakaways, and various detachment morphologies. These features typically exhibit bathymetric patterns that are roughly parallel to the accretion direction, positive Bouguer anomalies, and low seismic activity. Twelve Oceanic Core Complexes consistently occur at non-transforming discontinuities and asymmetric accretion segments. These mantle outcroppings indicate a low melt supply during the recent tectono-magmatic evolution of this region of the Mid-Atlantic Ridge.

Keywords: slow-spreading segment; detachment faults; oceanic core complexes; multi-beam bathymetry; sea-floor morphology; morpho-structural mapping

INTRODUCTION

Lower crustal and upper mantle ductilely deformed rocks are exhumed in the context of slow-spreading centers along the footwall of long-lived, large-offset, low-angle normal faults known as detachment faults (Whitney et al., 2013; Smith et al., 2014; Escartín et al., 2017). These massif exposures of deep-seated, high-temperature intrusive, and ultramafic rocks may occur anywhere along the length of an ocean ridge segment (Cannat et al., 2006; Smith et al., 2008). They are named oceanic core complexes (OCCs), a key feature to understand the thermal structure of the upper mantle, mechanisms of crustal accretion, evolution of young lithospheres, and hydrothermal systems (Schilling et al., 1995; Gràcia et al., 2000; Blackman et al., 2009; Peirce et al., 2019). First recognized in geophysical images at 30º N in the Mid-Atlantic Ridge (MAR; Cann et al., 1997), the OCCs have been mapped in several Non-Transform Discontinuities (NTDs) and are now considered a fundamental structure of sea-floor spreading at slow- and ultraslow-spreading ridges (Blackman et al., 2009; Whitney et al., 2013; Smith et al., 2014). Despite the advances in conducting scientific surveys on mid-ocean ridges, the study of OCCs remains limited to only a few areas in MAR, Caribbean–North American Ridge, Southwest India Ridge, and Australian-Antarctic Discordance (Dick et al., 2000; Smith et al., 2008; Hayman et al., 2011).

The OCCs are characterized by dome-shaped morphology on the sea-floor, with a short wavelength corrugated surface, structurally higher than the uppermost brittle fault surface. They present tens of kilometers of displacement in the shallowest parts of the rift shoulders (MacLeod et al., 2009). The hanging wall, positioned between the OCCs and the spreading axis, is affected by magmatic and hydrothermal activity. It can be covered by extrusive or rider blocks, or replaced by lithosphere-cutting faults (Cannat et al., 2006; Petersen et al., 2009; Reston and Ranero, 2011). The root of detachment faults is likely found in the magma chamber, where they exhibit high-angle characteristics. As the faults surface corrugate, they change into low-angle faults with parallel kinematics aligned to the extension direction. This transition is controlled by a rolling hinge that accommodates foot wall exhumation (Cann et al., 1997; Tucholke et al., 1998; Cannat et al., 2006; MacLeod et al., 2009). Moreover, tectonic uplift may result in low-angle faults that create dome-shaped morphologies, which are favored by the limited magmatic supply in segments of NTDs (Gràcia et al., 2000). At intermediate rates of magmatism and magma supply, the OCCs expose zones of ultramafic rocks undergoing brittle deformation and a wide ductile area of intrusive rocks at the ocean floor (Escartín et al., 2003; Schroeder and John, 2004). Furthermore, this morphology records thermal processes, such as hydration during serpentinization or mylonitization, associated with crustal thinning in extending lithosphere and serving as significant sites for magmatic heat input, mantle hydration, and mass transfer (Tucholke et al., 2008; Whitney et al., 2013).

Non-Transform Discontinuities (NTDs) are second to higher-order linear discontinuities that segment irregularly the spreading axis in intervals ranging from 10 to 100 km without noteworthy association with Transform Faults (TFs) (Sempéré et al., 1993; Tucholke et al., 1997; Zheng et al., 2019). The propagation of NTDs is linked to the stress field and rheology, which control tectonic jumps and ridge reorientation, as well as the increase in magma supply and interactions with hotspots

(Sempéré et al., 1993; Hey et al., 2010; Dannowski et al., 2018; Zheng et al., 2019). In the spreading center, NTDs create off-axis discordant zones that remain for a long time and accommodate horizontal shearing stresses through diverse morpho-tectonic expressions (Grindlay & Fox, 1992; Sempéré et al., 1993). NTDs show moderate to high seismic activity and a symmetric pattern of magnetic anomaly associated with sea-floor spreading. Generally, exhibit higher heat flow compared to surrounding areas due to the upwelling of hot mantle material, and due to density major gravity anomalies (McKenzie & Bickle, 1988; Rosencrantz et al., 1988; Karson & Rona, 1990; Chen, 2003). Therefore, NTDs are an important component of the tectonic processes occurring along the MAR (Grindlay & Fox, 1992).

The Equatorial MAR has been extensively studied for hydrothermalism, mineralization, seismicity, and mantle/lithosphere dynamics, but there are limited reports on OCCs morphology, structural patterns, and distribution (Udintsev, 1996; Mazarovich et al., 2001; Skolotnev et al., 2003, 2022, 2023; Savel'eva et al., 2006; 2008). This study investigates the OCCs along a 900 km of the ridge axis from Bogdanov Fracture Zone (7º 10' N) to Saint Paul Fracture Zone (0º 50' N). The dataset contains global bathymetry, gravimetry, seismicity, and new multi-beam bathymetry from geophysical cruises on the Equatorial MAR conducted by the Geological Survey of Brazil (Fig. 1). The primary goal is to map OCCs, comprehend distribution controls, and explore their relationship to NTDs, offering insights into the role of OCCs in Equatorial MAR segment development. This study enhances the understanding of the morpho-tectonic evolution of this part of the MAR.

Geological Setting of Study Area

The evolution of the northern Equatorial MAR, between the Equator and 15º N (Fig. 1A), was significantly shaped by long-lived mantle plume activity leaving the evidence on the ocean floor, such as the Demerara Plateau and Guinea Plateau at the continental margin, along with the aseismic rises of Ceara and Sierra Leone, during the Jurassic rifting and Cretaceous spreading of the Equatorial Atlantic (Basile et al., 2020). This mantle plume induced tectono-magmatic processes, from initial plume-driven volcanism during breakup to crustal stretching with mantle exhumation along the Equatorial MAR (Kilsdonk et al., 2024). Dredged samples of hotspot-related magmatic rocks indicate that the Sierra Leone hotspot track was responsible for the formation of these marginal/oceanic features and seamount chain over a period of 180 million years (Schilling et al., 1994; Basile et al., 2020; Kilsdonk et al., 2024). Sierra Leone mantle plume causes 1,600 km long geochemical anomaly, observed in the basalt glasses which contrast with different surrounding mantle sources and the southern zone of the Equatorial MAR (Schilling et al., 1994; Le Voyer et al., 2015).

According to Schilling et al. (1995) the segments of Equatorial MAR exhibit a cold and dense upper mantle belt. Moreover, heterogeneity of local mantle thermal conditions beneath the intra-transform spreading ridges segments reflects the enrichment and magma production in a partial melting depleted peridotite source; a local mantle upwelling; the influence of spreading rates; and the proximity of hot spots (Bonatti et al., 1992; Skolotnev et al., 2003; Savel'eva et al., 2004; Sani et al., 2024). The upper

mantle thermal minima might cause the long-lived transform cluster that segments the mid-ocean ridges (Bonatti, 1996; Udintsev, 1996). The mantle exhumation generally occurs on NTDs, which divide the ridge in en-chelon segments, ultramafic rocks and gabbros are frequently found on the walls of rift valleys, with basalts commonly on the flanks and valley floor (Savel'eva et al., 2006), while OCCs depends on variation of magma enrichment conditions, being spatially restricted and structurally isolated (Peirce et al., 2019).

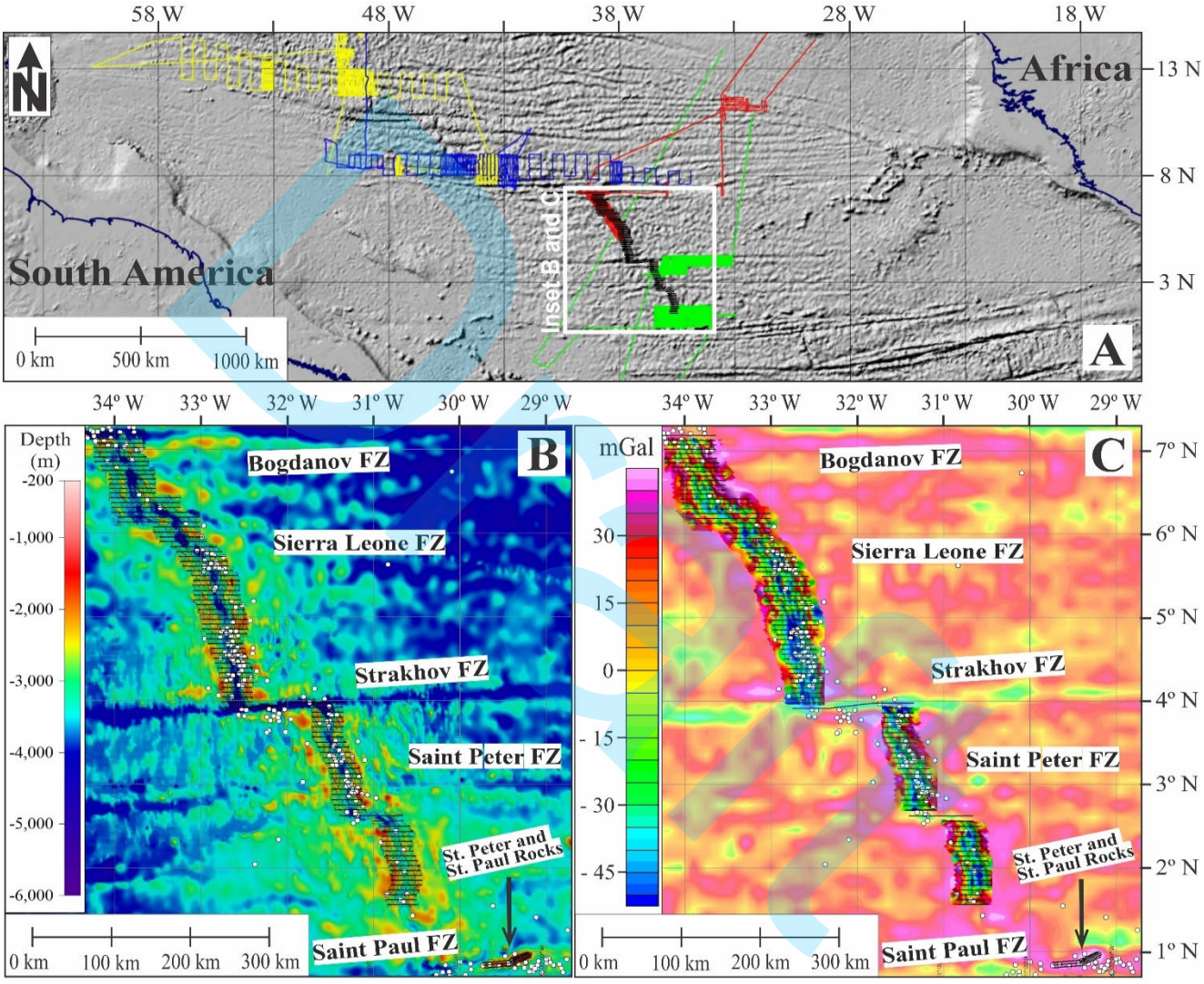

Figure 1 - A) Russian and Russian – Italian scientific expeditions on MAR with their respective cruise numbers shown by colors: 6 (yellow), 9 (blue), 12 (green), and 22 (red) of the R/V Akademik Nikolay Strakhov (adapted from Mazarovich et al., 2001). The study area of the Geological Survey of Brazil cruises is demarcated in the parallel black lines inside the black rectangle near 33°W and 4°N. B) Map of the high-resolution bathymetric survey (black lines) and the regional bathymetry (GEBCO, 2021). The white dots indicate the distribution of the earthquake epicenters (USGS, 2021). C) Bouguer anomaly map of the survey area overlay on regional free-air gravity anomalies derived from satellite altimetry (Sandwell et al., 2014). The white dots indicate the geographic distribution of earthquake epicenters (USGS, 2021).

The equatorial segment structure differs from those north and south surrounding segments of the ridge. The segments only feature a distinct spreading center within their narrow axial zone. In contrast, the morphology of the ridge flank appears mosaic-like, resembling a plateau more than a typical spreading system (Udintsev, 1996). Multiple regional faults show a complex geochronology and a varied relationship to other structures in the rift zone (Udintsev, 1996), whereas the ridge has an average spreading rate of about 2.5 cm/year (Fujiwara et al., 2003). The axial MAR domain is marked by 3 TFs (Bogdanov, Strakhov, and Saint Paul), and 12 NTDs (Tab. 1), which offset the axis by variable lengths (from 2 to 110 km), and along with the axial domain, two detachment faults located close to NTDs were mapped.

The study area is limited to the North by the ~600 km long Doldrums multi-fault transform system (Skolotnev et al., 2019, 2022, 2023; Sani et al., 2024), where there are several closely spaced transform faults (Bogdanov, Pushcharovskiy, Vernadskiy, and Doldrums). The southern limit of the study area corresponds to the 630 km long St. Paul Transform System, with four transform faults, offsetting three intra-transform ridge segments (Maia et al., 2016), where the Saint Peter and Saint Paul Archipelago rises ~ 4000 m surrounding sea-floor. Between these two large transform systems, roughly from 0º 50' N to 7º 10' N, the MAR axis is segmented by numerous higher-order discontinuities. The research area has four segments, delimited by transform faults (TF) and non-transform discontinuities (NTD), comprising the ridge segments between the Bogdanov TF to Sierra Leone TF (7º N Segment), Sierra Leone TF to Strakhov TF (5º N Segment), Strakhov TF to Saint Peter TF (3º N Segment), and Saint Peter TF to Saint Paul TF (2º N Segment) (Figs. 1 and 2).

METHODOLOGY

The Geological Survey of Brazil carried out marine geophysical surveys in 2012 and 2013 using the Ocean Stalwart research vessels along the axial zone of the Equatorial MAR. Multi-beam bathymetry, acoustic imagery, and gravity data were collected along major features of the MAR (Fig. 1), extending over 30 km on each side of the ridge axis. In addition, recorded earthquake epicenters from the United States Geological Survey catalog (USGS, 2021) in the region, from the global bathymetric data assembled by the General Bathymetric Chart of the Oceans (GEBCO, 2021), and free-air gravity anomalies derived from satellite altimetry (Sandwell et al., 2014) were incorporated into our dataset (Figs. 1B and 1C). The Global Mapper software was used to visualize the data, to analyze their morphological characteristics and distribution, and to interpret the structures of the ridge segments. The multi-beam echo-sounder (MBES) Teledyne RESON, model SeaBat 7150, was installed on the ship hull. This system works at a frequency of 12 kHz with up to 880 beams per ping. The data were stored in the raw s7k during acquisition with the PDS 2000 software and gridded with a cell size of 100 x 100 m using the Caris Hips and Sips software. Additionally, global data from GEBCO (2021) were used to complement the analysis of the regional relief in the study area.

Table 1 – List of morpho-structural segments between the Bogdanov Fracture Zone (7º 10' N) to Saint Paul Fracture Zone (0º 50' N).

Name	Location	Order	Offset (kilometers)	Segment	Depth (meter)
Bogdanov Transform Fault	7º 10' N	First	80	7ºN	3,500 - 5,000
Bogdanov Fracture Zone	7º 10' N	NA	NA	7ºN	3,500 - 5,000
Nontransform Offset	6º 50' N	Second	10	7ºN	3,500 - 4,100
Sierra Leone Fracture Zone	6º 15' N	NA	NA	7ºN	3,500 - 4,100
Nontransform Offset	6º 15' N	Second	50	7º/5ºN	3,500 - 4,100
Nontransform Offset	5º 54' N	Second	8	5ºN	3,000 - 5,000
Nontransform Offset	5º 47' N	Second	15	5ºN	3,500 - 4,500
Lower-order displacement	5º 31' N	Third or Fourth	2	5ºN	3,500 - 4,000
Lower-order displacement	5º 06' N	Third or Fourth	3	5ºN	3,900 - 4,100
Nontransform Offset	4º 40' N	Second	7	5ºN	3,400 - 3,800
Lower-order displacement	4º 26' N	Third or Fourth	3	5ºN	3,800 - 4,600
StrakhovTransform Fault	3º 55' N	First	110	5ºN/3ºN	4,000 - 5,000
Strakhov Fracture Zone	3º 55' N	NA	NA	5ºN/3ºN	4,000 - 5,000
Nontransform Offset	3º 30' N	Second	8	3ºN	3,500 - 4,000
Nontransform Offset	3º 10' N	Second	5	3ºN	3,600 - 4,100
Saint Peter Fracture Zone	2º 36' N	NA	NA	3ºN/2ºN	2,700 - 4,200
Nontransform Offset	2º 36' N	Second	33	3ºN/2ºN	2,700 - 4,200
Lower-order displacement	2º 03' N	Third or Fourth	3	2ºN	3,000 - 3,600
Nontransform Offset	1º 40' N	Second	9	2ºN	3,000 - 3,500
Saint Paul Transform Fault	0º 50' N	First	300	2ºN	0 - 5,000
Saint Paul Fracture Zone	0º 50' N	NA	NA	2ºN	3,500 - 5,000
				NA = Not Applicable	

The gravimeter installed onboard was an Air-Sea System II, model S-145 manufactured by Micro-G LaCoste. This model is a spring tension gravity meter, mounted on a dynamically stable platform, which allows its use on ships and airplanes. The data were acquired with a frequency of 1 Hz. The processing removed spurious data and spikes, base transfer, instrumental drift, tidal drift correction, latitude correction, Eötvös correction, and finally obtaining free-air and Bouguer anomalies (Fig. 1C). The residual isostatic anomaly was calculated by the compensation root Airy model using vertical density contrasts between oceanic crust and upper mantle of 0.4 kg/m^3, being 2.9 g/cm^3 for oceanic crust and 3.3 g/cm^3 for the upper mantle (Blakely, 1996). The depth of the Mohorovičić discontinuity (about 10 km) and the depth of the base of the isostatic compensation root (between 8 and 9 km) were estimated based on the isostatic model (Simpson et al., 1983). Data were gridded with cell size defined as 1/4 of the acquisition line spacing (6 - 7 km), using the minimum curvature method (Smith and Wessel, 1990). The gravimetry data were processed in the Oasis Montaj software (Geosoft, 2008).

Additionally, free-air gravity anomalies derived from satellite altimetry (Sandwell et al., 2014) and seismicity data (Fig. 1C) were used to support regional interpretations of the main structures and morphologies present in the research area and to understand the continuity of structures that affect the ridge axis morphology. The local distribution of the earthquake epicenter (USGS, 2021) was used to correlate of seismicity with the interpretations of morphological features, especially in the inferences of OCCs, on a regional segment scale.

RESULTS

The main results were the segmentation of the ridge axis into fundamental tectonic units delineated by transform faults (TF) and non-transform discontinuity (NTD) of the ridge axis in its fundamental unit of segments (Tab. 1), which enables a detailed assessment of morphological variability at the segment scale. Traces of the TFs, Fracture Zones (FZs), and extensions of Oceanic Core Complexes (OCCs) (Tables 1 and 2) beyond the bounds of high-resolution bathymetry coverage area were interpreted using global predicted bathymetric data (GEBCO, 2021) (Fig. 2). This approach confirmed the regional continuity of these tectonic structures, especially the FZs, across the ridge. The geophysical data (multi-beam bathymetry, backscatter, slope, and Bouguer anomaly) further allowed for precise mapping of these features internal to the axial rift valley of the ridge segments, including ridge axis, the axial rift valley itself, axial volcanic ridge (AVR), normal faults, the nodal basins, and sedimented basins (Figs. 3 to 10), which revealed the structural framework and main morpho-tectonic elements of the ridge segments.

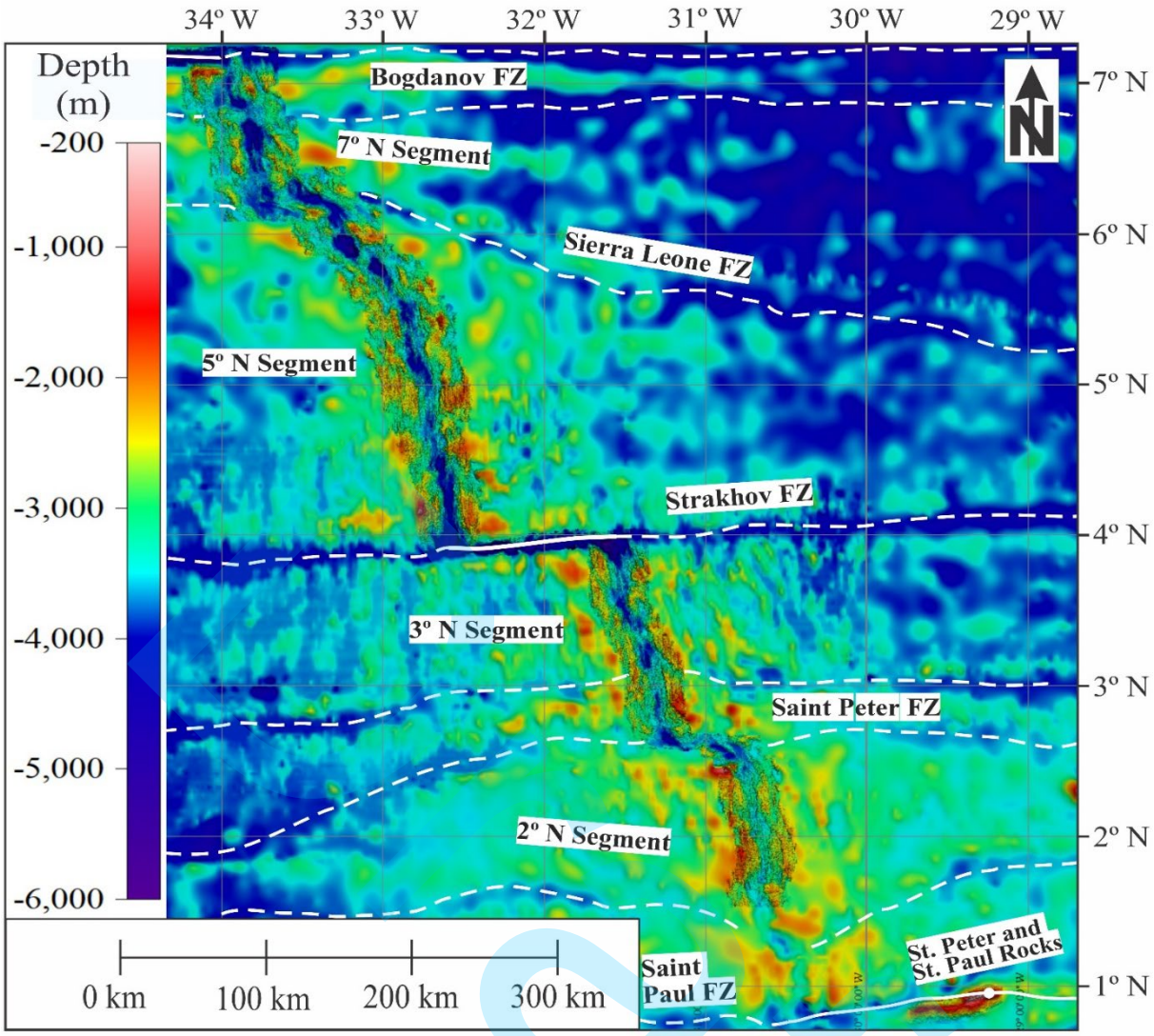

Figure 2 - Multi-beam bathymetry data survey in the project, over GEBCO (2021) bathymetry data. The solid white lines are the transform faults, the dashed white lines are the fracture zones, and the green dashed lines are the delineation of the extent of the oceanic core complex.

Table 2 - Characteristics of OCCs in the Equatorial MAR.

OCC	Segment	Active	Associeted Feature	Flank	Shape	Corrugation	Size (km)	Backscatter (decibels)	Depth (meters)	Slope (alignment)	Anomaly Bouguer	Seismicity
7° N	7° N	Yes	TF	West	Dome	Yes	25 X 12	high	1,400	parallel	positive and negative	high
6° 58' N		Yes	NTD	East	Dome	No	13 X 10	high	1,750	parallel	positive and negative	low
6° 46' N		Yes	NTD	West	Dome	No	18 X 10	high	2,700	parallel	negative	low
6° 36' N		No	NTD	East	Dome + Ridge	No	25 X 13	high	2,200	parallel	positive	low
6° 21' N		Yes	NTD	East	Dome + Ridge	No	15 X 10	high	2,200	parallel	negative	low
6° N	5° N	Yes	NTD	East	Dome	No	30 X 12	high and low	2,000	parallel	positive and negative	low
4° 46' N		Yes	NTD	East	Dome	No	28 X 12	high and low	2,500	parallel	positive and negative	high
3° 43' N	3° N	No	NTD	East	Dome + Ridge	No	20 X 10	high and low	2,000	parallel	positive and negative	moderate
3° 23' N		Yes	NTD	East	Dome	No	17 X 12	high and low	2,000	parallel	positive	moderate
2° 40' N		Yes	NTD	East	Dome + Ridge	No	40 X 12	high and low	1,500	parallel	positive and negative	moderate
2° 20' N	2° N	No	NTD	West	Dome	No	30 X 10	high and low	800	parallel	positive	low
1° 36' N		Yes	NTD	East	Dome	Yes	33 X 33	high and low	2,000	parallel	positive	low

Bogdanov FZ to Sierra Leone FZ – 7º N Segment

The 7º N Segment spans approximately 110 km and is subdivided by a NTD into two distinct axial subsegments (Fig. 3). At the northern boundary of the segment, the Bogdanov TF offsets the ridge axis 80 km eastward, while another NTD, near 6º 15' N, shifts it 50 km to the east (Figs. 1, 2, 3, and 11; Table 1). Normal fault traces show high backscatter reflectivity (Fig. 3), and slopes greater than 10º occur in the major normal and detachment faults (Fig. 3). Only the OCC at 6º 36' N shows a positive Bouguer anomaly (Table 2).

The northern subsegment displays a 35 km long and 5-15 km wide rift valley, with an average water depth of 3,500 m, and the ridge axis has a sinuous shape. Its central part has an Axial Volcanic Ridge (AVR) spanning 1-4 km in width and rising 500 m above the seafloor (Fig. 3). Three dome-shaped structures 7º N, 6º 58' N, and 6º 46' N alternate between the flanks of the segment (Figs. 3 and 4). The highest concentration of normal faults is on the northern part of the eastern flank, with N-S direction (Fig. 3). The northern ridge subsegment shifts the axis of the ridge 10 km to the east (Tab. 1).

The southern subsegment extends approximately 70 km with a 5-15 km wide rift valley, in an average water depth of 4,000 m, and an approximate N-S direction. Its central part, the AVR are 1-2 km wide rising 200 m high. OCCS were named 6º 46' N, 6º 36' N, and 6º 21' N, occurring on both flanks of this subsegment (Figs. 3 and 4). In the southern portion of the ridge segment, six small sedimentary basins elongate in the NW-SE direction with few tens of kilometers long and a few kilometers wide. These basins are associated with the NTD boundaries of this subsegment. The ridge axis is displaced 50 km to the east by this NTD (Fig. 3). The main faults trend NW-SE and have major distribution on the western flank.

The 7º N OCC has a dome-shaped structure on the eastern and north flank defining a 25 x 12 km-wide corrugated surface inside corner south of the Bogdanov TF (Figs. 3 and 4A). This structure is elongated parallelly to the spreading for 25 km, has a width of 12 km, and rises from the valley floor over 2,000 m (Figs. 3 and 4A), with the summit approaching 1,400 m water depth. It also has two extensions in the ridge form at the south side, with a length of approximately 20 km, which probably correspond to the OCC breakaway. It ends in the axial rift valley, in contact with the axial volcanic ridge.

The OCC 6º 58' N is a dome-shaped structure at the junction of the ridge segment and the 6º 50' N NTD, in the eastern flank of the ridge segment (Figs. 3 and 4B). This structure is elongated parallelly to the axial rift valley by 13 km, has a width of 10 km, and rises from the valley floor almost 1,800 m (Figs. 3 and 4B), with the summit at water depths of 1,750 m.

The OCC 6º 46' N is a ridge-shaped structure at the junction of the ridge segment and the 6º 50' N NTD, in the western flank of the ridge segment (Figs. 3 and 4C). This structure is elongated parallelly to the rift valley for 18 km, has a width of 10 km, and rises from the bottom of the central rift for almost 1,000 m, summit reaches 2,700 m water depth.

The 6º 36' N OCC is a ridge-shaped structure of direction NW-SE, located an average of 15 km away from the axial rift valley, in the eastern flank of the dorsal segment (Figs. 3 and 4). This OCC is associated with an inactive detachment fault related to the NTD. This structure is elongated parallel to

the rift valley for 25 km, has a width of 13 km, and rises from the valley floor for almost 2,000 m (Figs. 3 and 4D), with the summit reaches 2,000 m water depth.

The 6º 21’ N OCC is a dome-shaped structure located at the junction of the ridge segment and the 6º 15’ N NTD, in the eastern flank of the ridge segment, represents an inner corner high (Figs. 3 and 4). This structure is elongated parallel to the rift valley for 15 km, has a width of 10 km, and rises from the bottom of the central rift for over 1,500 m (Figs. 3 and 4), with a summit approaching a water depth of 2,200 m. It also has a 25 km long northern ridge extension in the north side.

NTDs influence ridge segmentation and detachment geometries, fragment the Axial Volcanic Ridge (AVR) and make detachment faults oblique (Figs. 3 and 4). Ridge structures, including the ridge axis, AVR, rift valley, the normal faults, the nodal basins, and sedimentary basins, are all oriented in the NW-SE direction (Fig. 4).

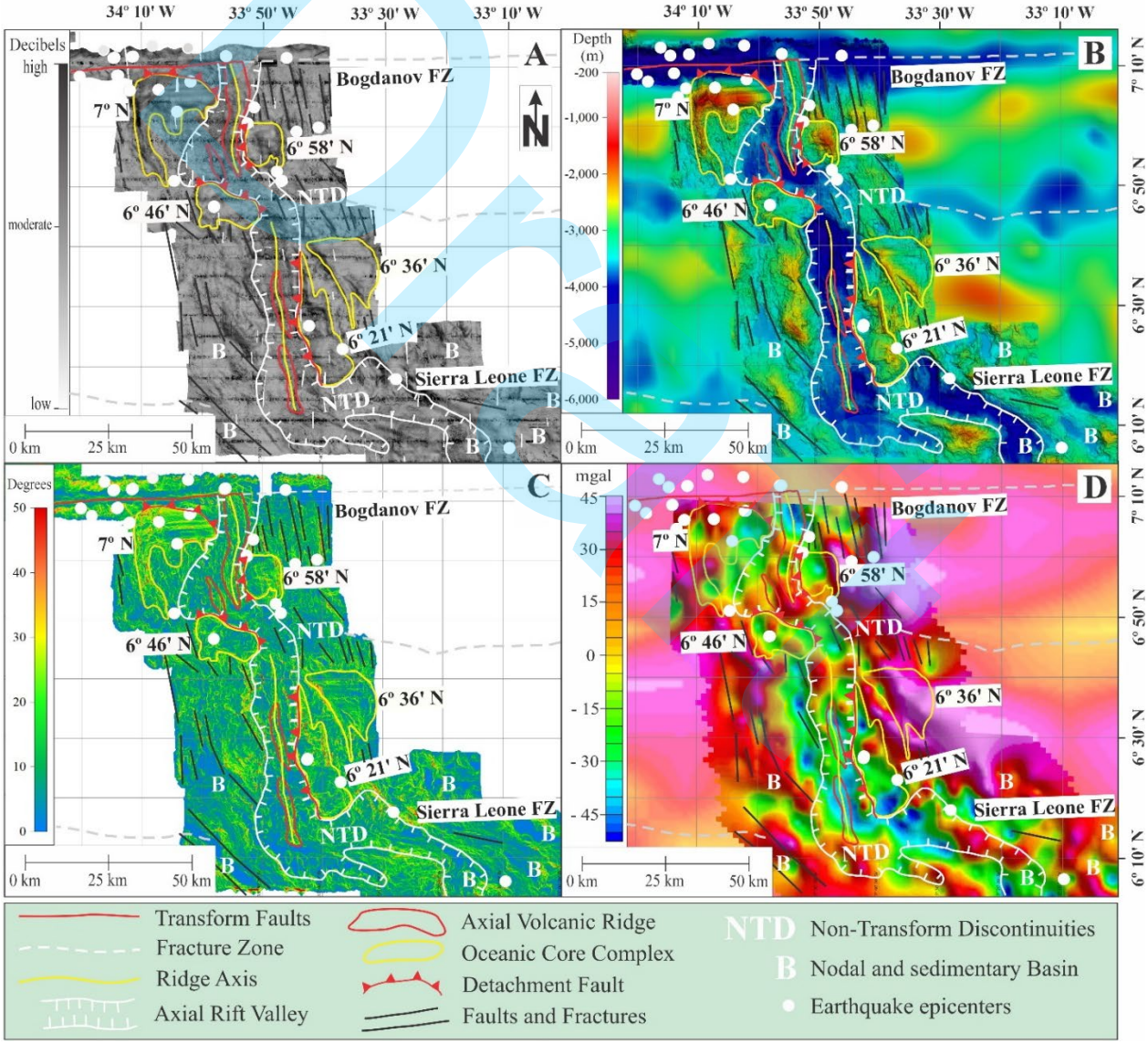

Figure 3 - Geophysical maps of the 7º N Ridge Segment between Bogdanov FZ to Sierra Leone FZ. A) Map of acoustic backscatter intensity of the sea-floor. B) High-resolution bathymetry map. C) Slope map. D) Bouguer anomaly map. Spatial distribution of earthquake epicenters is shown as white dots on maps (USGS, 2021).

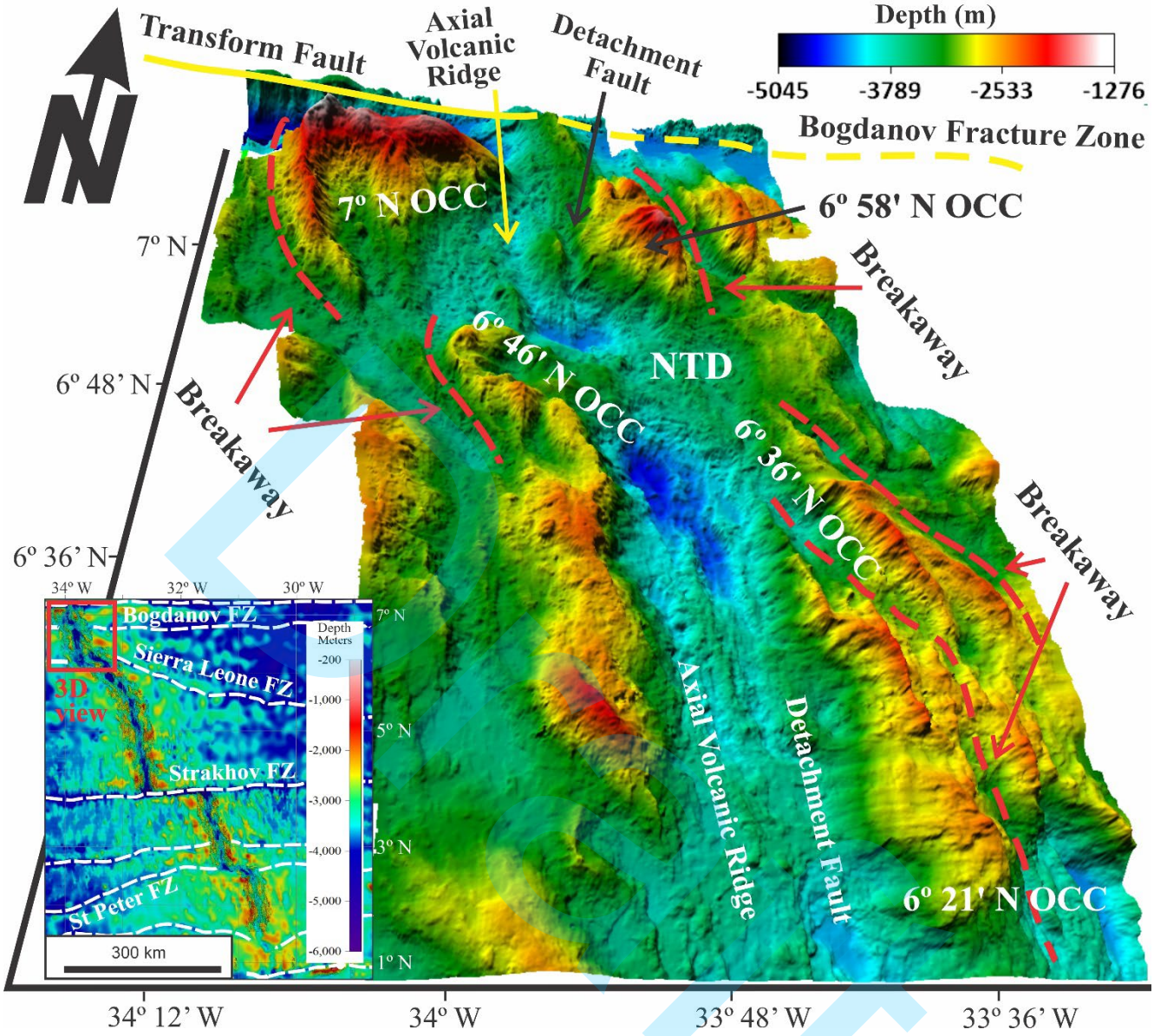

Figure 4 - 3D view of the 7º N Segment with 3 times vertical exaggeration.

Sierra Leone FZ to Strakhov FZ – 5º N Segment

The 5º N Segment extends approximately 310 km rift valley and is subdivided by a six NTDs into seven morphologically distinct ridge subsegments (Figs. 5, 6, and 11). At its southern boundary, the Strakhov TF (3º 55' N), offsets the ridge axis 110 km to the east, delimiting the segment to the south. Normal fault traces presenting high reflectance and slopes are greater than 10º characterizing the major fault scarps (Fig. 5). The positive Bouguer anomalies associated with OCCs progressively shift northeastward along the segment.

The first segment is only 12 km long and lies at 3,750 m average water depth. It lacks distinct rift valley, instead hosts a broad AVR (3-4 km wide), 300 m high, aligned in the N-S direction (Figs. 5 and 6). The normal faults are sparce in this segment.

The rift valley of the second ridge segment is also well marked. It features the rift morphology with a 28 km long and 7-12 km wide rift valley at an average water depth of 4,000 m. The ridge axis trends NW-SE. A 20 km long and 6 km wide sedimentary basin lies on the east flank, also NW-SE aligned. No AVR is observed in central part (Figs. 5 and 6). The segment displays asymmetric accretion, with the OCC named 6º N, a 30 x 10 km dome-shaped structure located on the east flank and dipping westward under the axial rift valley (Figs. 5 and 6). The normal faults remain limited in this segment.

The third segment spans 15 km long with an average water depth of 3,250 m (Figs. 5 and 6). Instead of a defined rift valley, it features an axial dome 8 km long, 5 km wide, and 400 m high. The ridge axis trends NW-SE (Figs. 5 and 6). The normal faults are scarce in this segment.

The fourth segment is 28 km long and 12 km wide, with a rift valley averaging 3,250 m water depth (Figs. 5 and 6). Its central part contains a 2-4 km wide, 200 m high AVR. The ridge axis trends NW-SE. Symmetric accretion is unclear, because of the absence of hills and faults perpendicular to the propagation direction (Figs. 5 and 6).

The fifth segment displays a 47 km long and 12 km wide rift valley (Figs. 5 and 6), with an average water depth of 3,500 m. Its central part contains a narrow (1-2 km), 300 m high AVR. Symmetric accretion is unclear, due to the small number of hills and faults perpendicular to the propagation direction.

The sixth segment displays a 75 km long and 10 km wide rift valley (Figs. 5 and 6), with an average water depth of 3,750 m. Its central part hosts a narrow AVR (1-2 km, 200 m high). The ridge axis is in NW-SE direction and displays asymmetric accretion by the OCC named 4º 46’ N, an embedded 20 x 10 km dome-shaped structure on the east flank, dipping westward under the axial rift valley (Figs. 5 and 6). The normal faults are predominantly N-S oriented.

The seventh segment is 62 km long, with an axial depth of 4,000 m, NW-SE oriented, and has an 8 km wide rift valley without ARV (Figs. 5 and 6). Oceanic fabric, typical of volcanic sea-floor, characterizes both sides of the rift valley, forming lineated hills and faults perpendicular to the spreading direction. This segment exhibits clear symmetric accretion with normal faults trending N-S (Figs. 5 and 6).

The 6º N OCC is a dome-shaped structure between two NTDs (6º 15’ N and 6º 05’ N) in the eastern flank of the dorsal segment (Figs. 5 and 6). This structure is elongated in the NW-SE direction for 30 km, has a width of 12 km, and rises 2,500 m from valley floor. Summit approaching a depth of 2,000 m (Figs. 5 and 6).

The 4º 46’ N OCC is a dome-shaped structure in the central part of the segment in the eastern flank of the dorsal (Figs. 5 and 6). This structure is 28 x 12 km, NE-SW elongated, and rises 1,500 m from the valley floor to 2,500 m water depth (Figs. 5 and 6). It lies between two bathymetric highs, to the south and north on the eastern flank of the segment, where this structure breaks the symmetrical accretion pattern (Figs. 5 and 6).

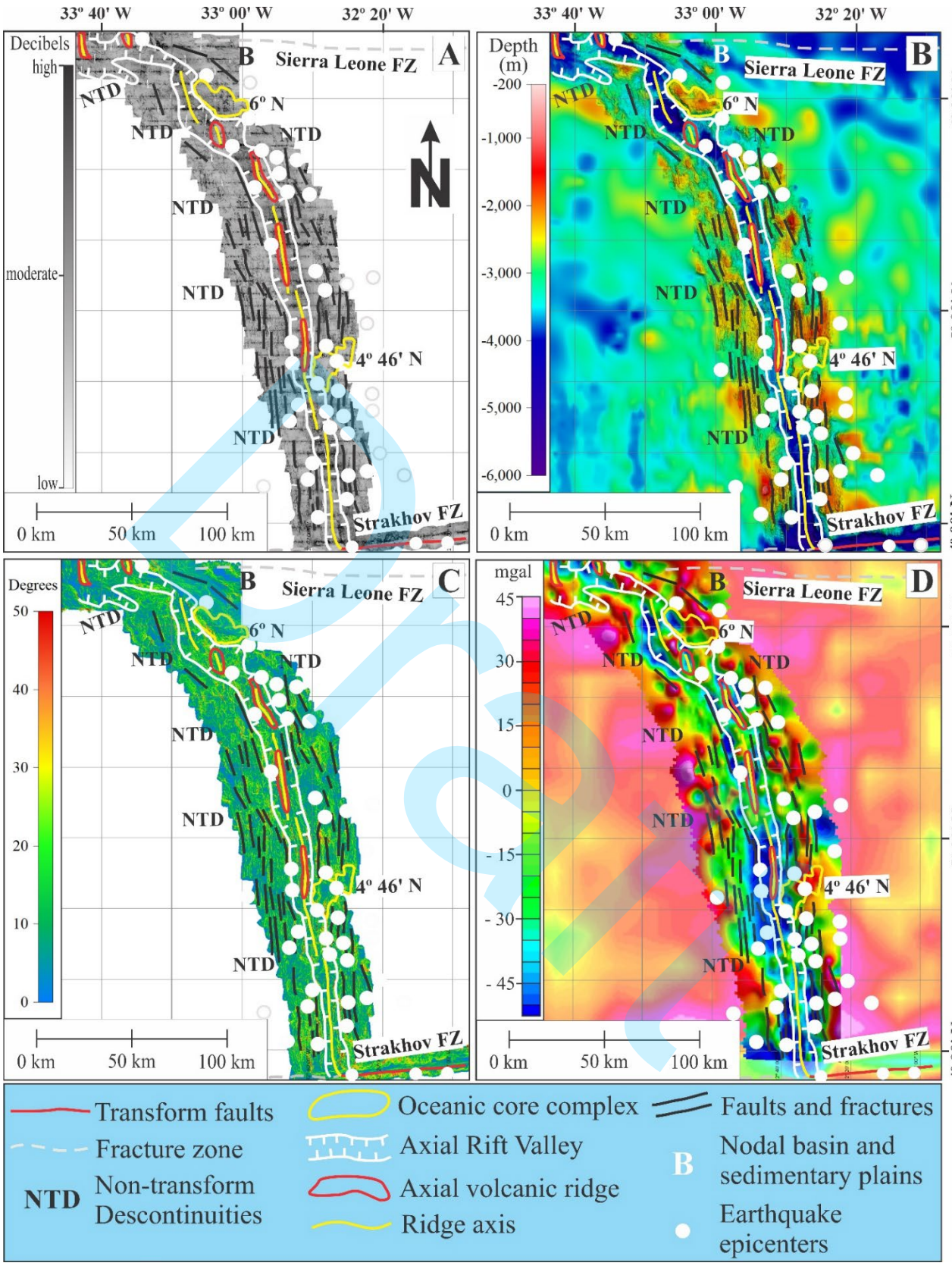

Figure 5 - Geophysical maps of the 5º N Ridge Segment between Sierra Leone FZ to Strakhov FZ. A) Map of acoustic backscatter intensity of the sea-floor. B) High-resolution bathymetry map. C) Slope map. D) Bouguer anomaly map. Spatial distribution of earthquake epicenters is shown as white dots on maps (USGS, 2021).

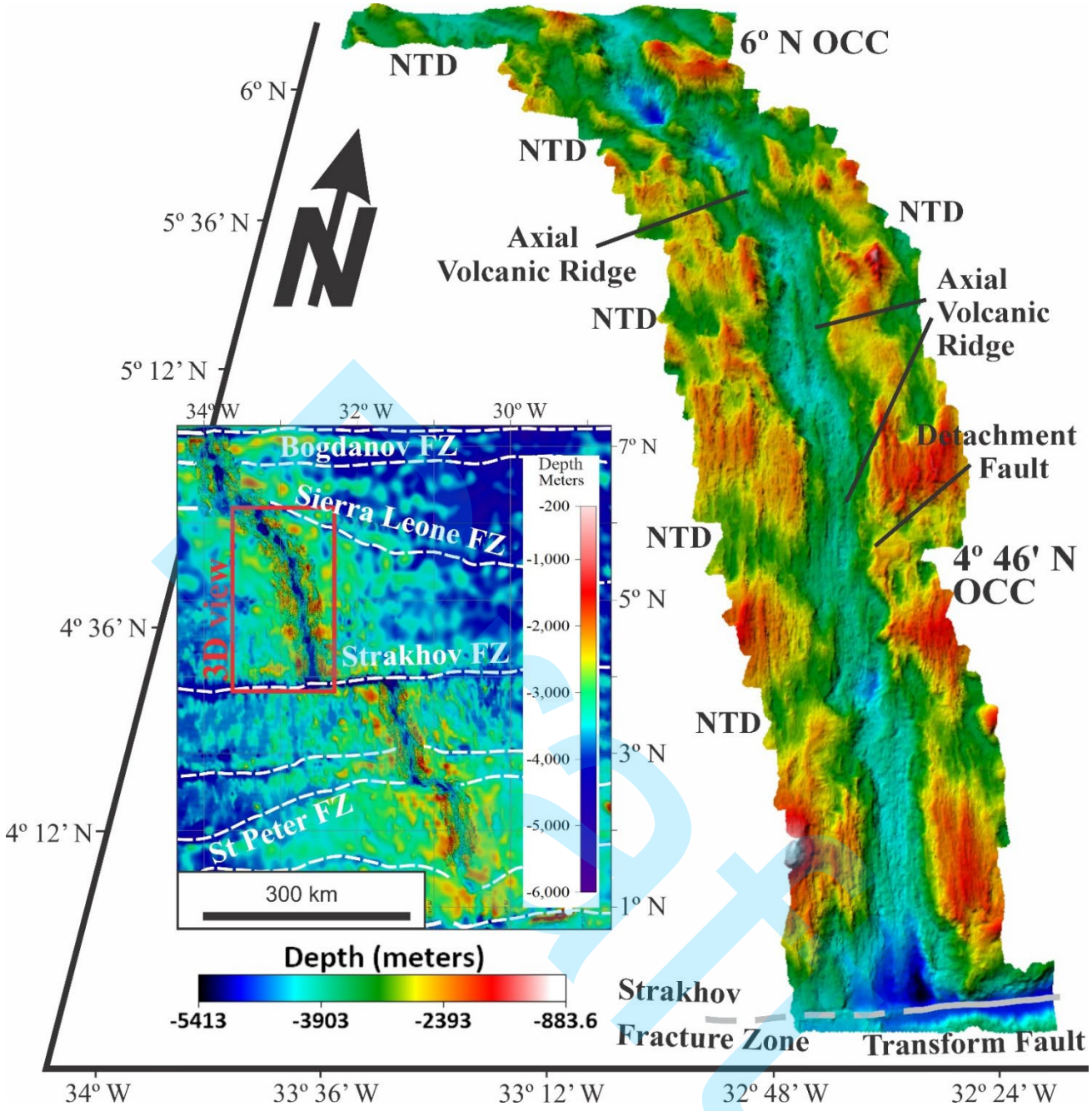

Figure 6 - 3D view of the 5º N Segment with 3 times vertical exaggeration.

Strakhov FZ to Saint Peter FZ – 3º N Segment

The 3º N Segment spans 160 km and is subdivided by two NTDs into three morphologically similar sub-segments (Figs. 7, 8, and 11). Seismicity in this region is low. High backscatter intensity is associated with normal faults and the axial rift valley, while slopes exceeding 10º appear in the major normal fault scarps (Figs. 7 and 8). The positive Bouguer anomalies are centered on the OCCs.

The north sub-segment extends 60 km N-S oriented, with an average water depth of 3,750 m, has a 4-10 km wide rift valley (Figs. 7 and 8). Its central part contains a narrow (1-2 km), 200 m high AVR. It has an asymmetric accretion by the embedded 20 x 10 km dome-shaped structure named 3º 43' N, on the east flank dipping westward under the axial rift valley (Figs. 7 and 8). The west flank is characterized

by hills and faults perpendicular to the spreading direction, predominantly NW-SE oriented. It has a nodal basin at the northern boundary, at the junction with the Bogdanov ZF (Figs. 7 and 8).

The central subsegment comprises a 30 km long and 6-10 km wide rift valley trending NW–SE, with an average water depth of 3,500 m (Figs. 7 and 8). Its axial zone hosts a narrow and sinuous AVR, measuring 0.8-1.5 km in width and rising 200 m above the valley floor. The subsegment exhibits an asymmetric accretion by the embedded 17 x 12 km dome-shaped structure named 3º 23' N OCC on the east flank, which dips westward under the axial rift valley (Figs. 7 and 8). The west flank is dominated by hills and fault patterns that are perpendicular to the spreading direction, with oblique faults trends NW-SE oriented (Figs. 7 and 8). The normal faults follow similar NW-SE alignments.

The south subsegment extends 65 km in the NW-SE direction, with a rift valley width of 5-10 km (Figs. 7 and 8) with an average water depth of 3,400 m. Its central part contains two narrow neovolcanic ridges (0,8-1,5 km wide, 250 m high). Asymmetric accretion dominates the eastern flank with a westward dip under the axial rift valley. This is the embedded 40 km x 12 km dome-shaped structure named 2º 40' N OCC (Figs. 7 and 8). In the west flank, the hills and faults are predominantly perpendicular to the spreading, but NW-SE oblique faults are also present (Figs. 7 and 8). The normal faults remain consistent with the NW-SE structural trend.

The 3º 43' N OCC is located 5 km east of the axial valley in the eastern flank of the 3º N Segment (Figs. 7 and 8). This dome-shaped structure spans 20 km along the rift valley, with a width of 10 km, and a vertical relief exciding 1,500 m in an inactive detachment fault. The summit reaches a water depth of 2,000 m.

The 3º 23' N OCC is a dome-shaped structure situated between two NTDs (3º 30' N and 3º 15' N) in the eastern flank of the dorsal segment (Figs. 7 and 8). This 17 x 12 km dome rises ~2,000 m from the rift floor aligned to the rift valley. It also has an elongated plateau measuring 8 x 6 km.

The 2º 40' N OCC is at the southern terminus of the 3º N Segment, in contact with the Saint Peter FZ (Figs. 7 and 8). This dome-shaped structure extends 40 km along the eastern flank parallel to the rift valley. This structure has a width of 12 km and rises 2,000 m above the axial valley floor, with its summit reaching 1,500 m water depth.

Saint Peter FZ to Saint Paul FZ – 2º N Segment

The 2º N Segment comprises a 220 km long rift valley divided by one NTD into two morphologically similar subsegments (Figs. 9, 10, and 11). At the north boundary, near the Saint Peter FZ (2º 36' N), a NTD offsets the ridge axis approximately 50 km eastward (Figs. 1, 2, 9, and 10). The south boundary a NTD (1º 40' N) marks the south limit, shifting the ridge axis 8 km eastward (Figs. 1, 2, 9, and 10).

The north subsegment spans 110 km long, with a rift valley 4-10 km wide and an average water depth of approximately 3,750 m (Figs. 9 and 10). The ridge axis has a sinuous shape and trends NW-SE. An AVR, 1-3 km wide and, 300 m high, occupies the central region. Asymmetric accretion is evident along the west flank, where the 2º 20' N OCC, a dome-shaped structure measuring 30 x 10 km, dips eastward

under the axial rift valley (Fig. 9). The eastern flank exhibits ridge-perpendicular hills and fault systems, while nodal basins and sedimentary basins, oriented NW-SE, are distributed across the northern end and central portion of the segment (Figs. 9 and 10). The normal fault trends also align NW-SE.

The south subsegment measures 20 km in length and 8 km in width, with an average water depth of 3,400 m (Figs. 9 and 10). The ridge axis has NW-SE direction. No AVR is observed in the axial zone. Asymmetric accretion is indicated by the 1°36′N OCC, 18 x 12 km dome-shaped structure on the east flank dipping westward under the axial rift valley (Figs. 9 and 10). The western flank features hills and faults lineations perpendicular to the spreading direction. Satellite-derived bathymetry and gravity data suggest this OCC extends 30 km southeastward (Figs. 1 and 9). Fault orientations throughout both subsegments predominantly follow the NW–SE structural trend.

The 2º 20’ N OCC is located on the western flank, approximately 10 km away from the axial rift valley, associated with an inactive detachment fault (Figs. 9 and 10). This dome-shaped structure extends 30 km parallel to the rift valley, has a width of 10 km, and rises 3,000 m above the valley floor (Figs. 9 and 10), with a summit reaching the depth of 800 m.

The 1º 36’ N OCC is located in the southern portion of the segment adjacent to the 1º 40’ N NTD, occupying the inner corner high (Figs. 9 and 10). This dome-shaped structure shows the corrugations surface elongated parallel to the rift valley for 18 km, has a width of 12 km, rises 2,500 m from rift valley floor (Figs. 9 and 10), and reaches a summit depth of 2,000 m. GEBCO (2021) bathymetry data suggests a structural continuation 30 km in the NW-SE direction (Fig. 9).

Seismicity

Low seismicity is observed in the 7º N Segment, the northern portion of the 5º N Segment, and the 2º N Segment. High seismicity characterizes the central area between the 5º N and 3º N Segments. In general, according to Sokolov et al. (2016), the seismic activity follows the typical distribution of slow-spreading ridges, with earthquake epicenters localized along parts of the mid-ocean ridge and transform faults, as observed in the present study (Figs. 3, 5, 7, and 9). The low seismicity of the 7º N Segment, from the initial part of the 5º N Segment and the 2º N Segment, are correlated with occurrences of OCCs, thus suggesting a tectonically active region.

Gravity Bouguer Anomalies

Positive Bouguer anomalies (exceeding +30 mgal) are preferentially centered on the eastern flank of the ridge (Figs. 3, 5, 7, and 9), aligned with NW-SE-trending oblique faults. In contrast, negative Bouguer anomalies (below -15 mgal) are centered and aligned to the axial rift valley (Figs. 3, 5, 7, and 9), concordant with the accretion axis of the ridge. The positive anomalies are predominantly on inner corner highs, especially those exhibiting corrugated surfaces. This pattern is commonly associated with OCCs, as described by Sokolov et al. (2016), and indicates the exhumation of high-density, deep-seated rocks within OCCs. Conversely, the rift valley is underlain by lower-density crustal material, consistent with its role as a site of active magmatic accretion.

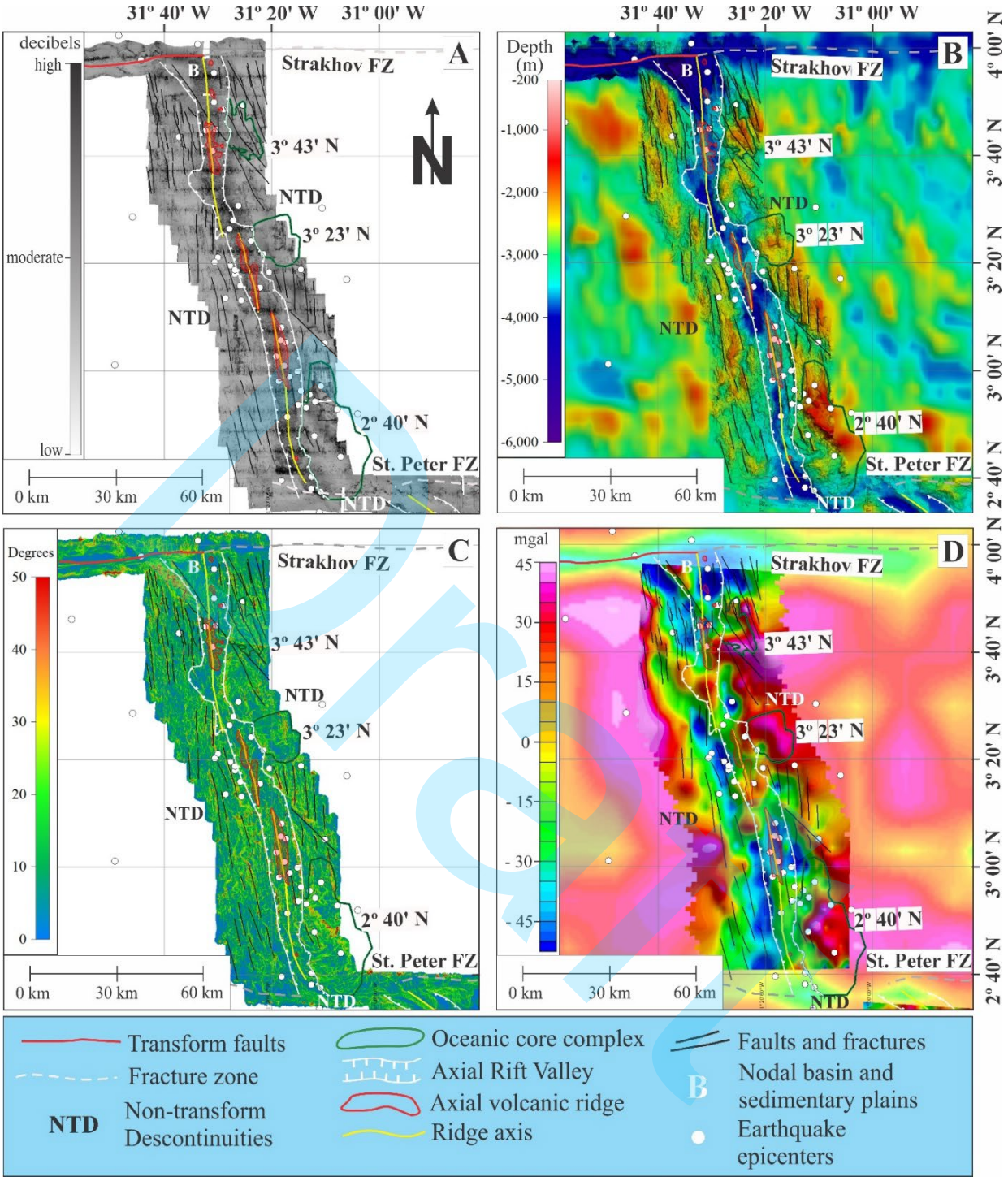

Figure 7 - Geophysical maps of the 3º N Ridge Segment between Bogdanov FZ to Sierra Leone FZ. A) Map of acoustic backscatter intensity of the sea-floor. B) High-resolution bathymetry map. C) Slope map. D) Bouguer anomaly map. Spatial distribution of earthquake epicenters is shown as white dots on maps (USGS, 2021).

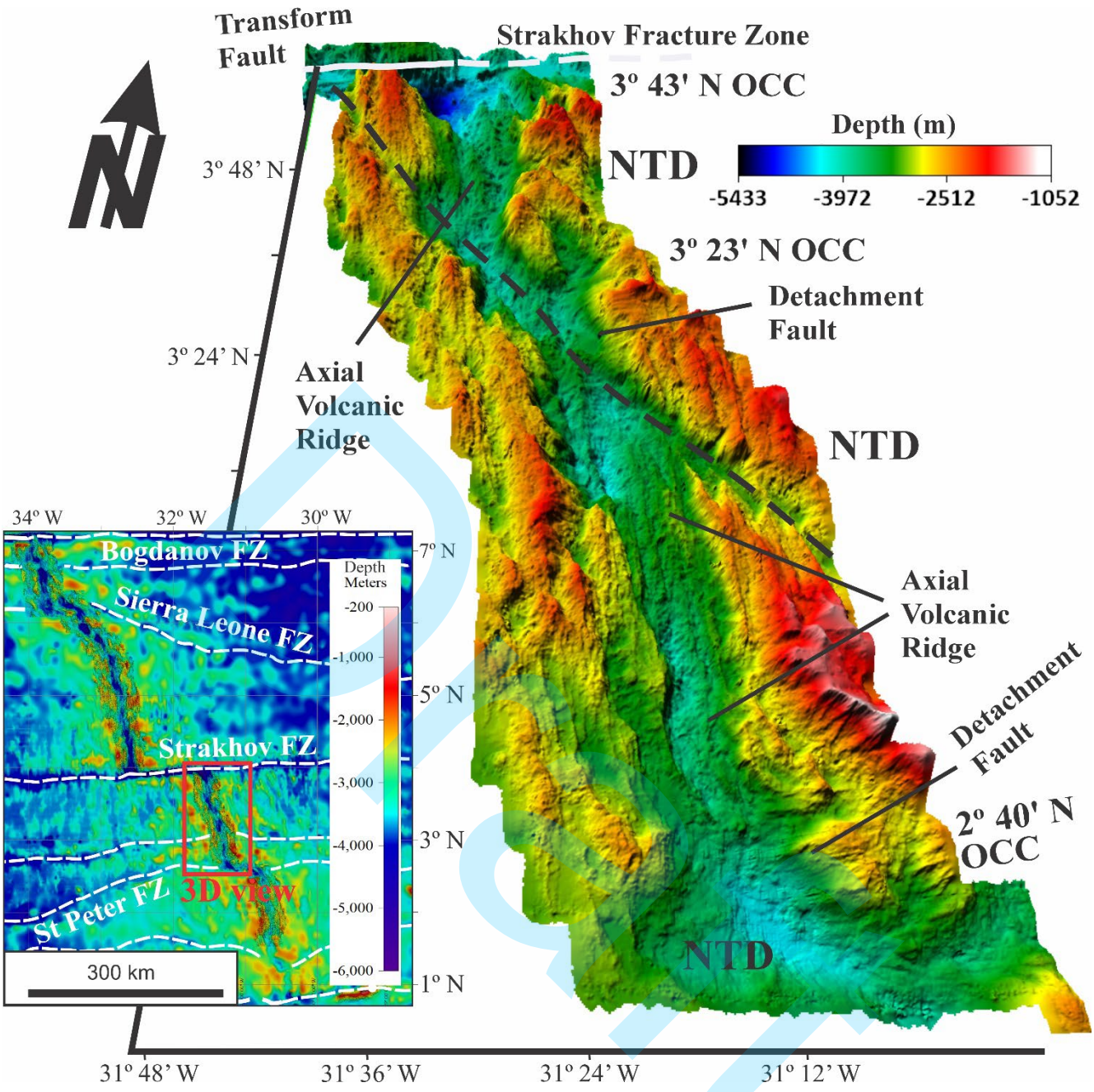

Figure 8 - 3D view of the 3º N Segment with 3 times vertical exaggeration.

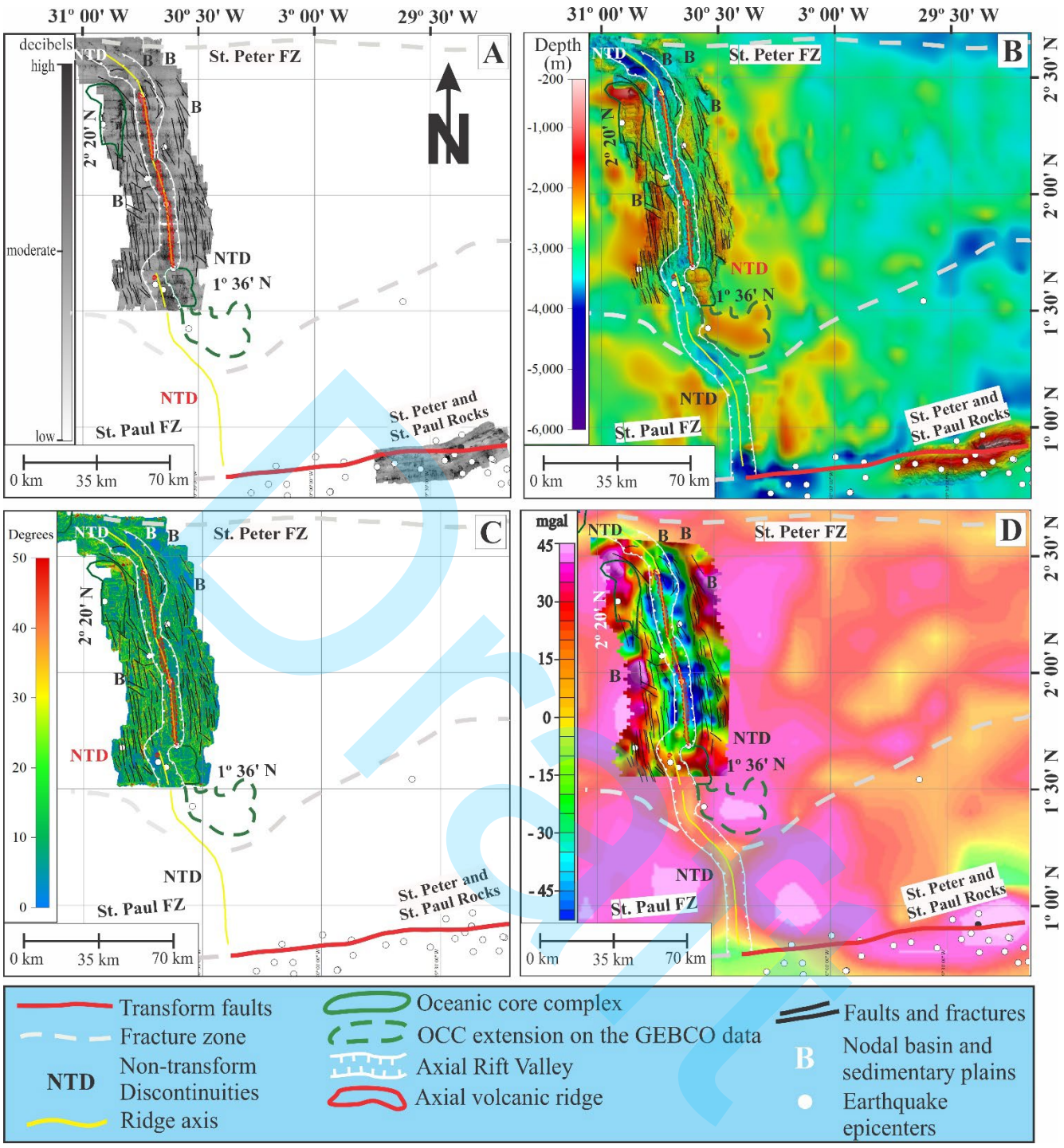

Figure 9 - Geophysical maps of the 2º N Ridge Segment between Saint Peter FZ to Saint Paul FZ. A) Map of acoustic backscatter intensity of the sea-floor. B) High-resolution bathymetry map. C) Slope map. D) Bouguer anomaly map. Spatial distribution of earthquake epicenters is shown as white dots on maps (USGS, 2021).

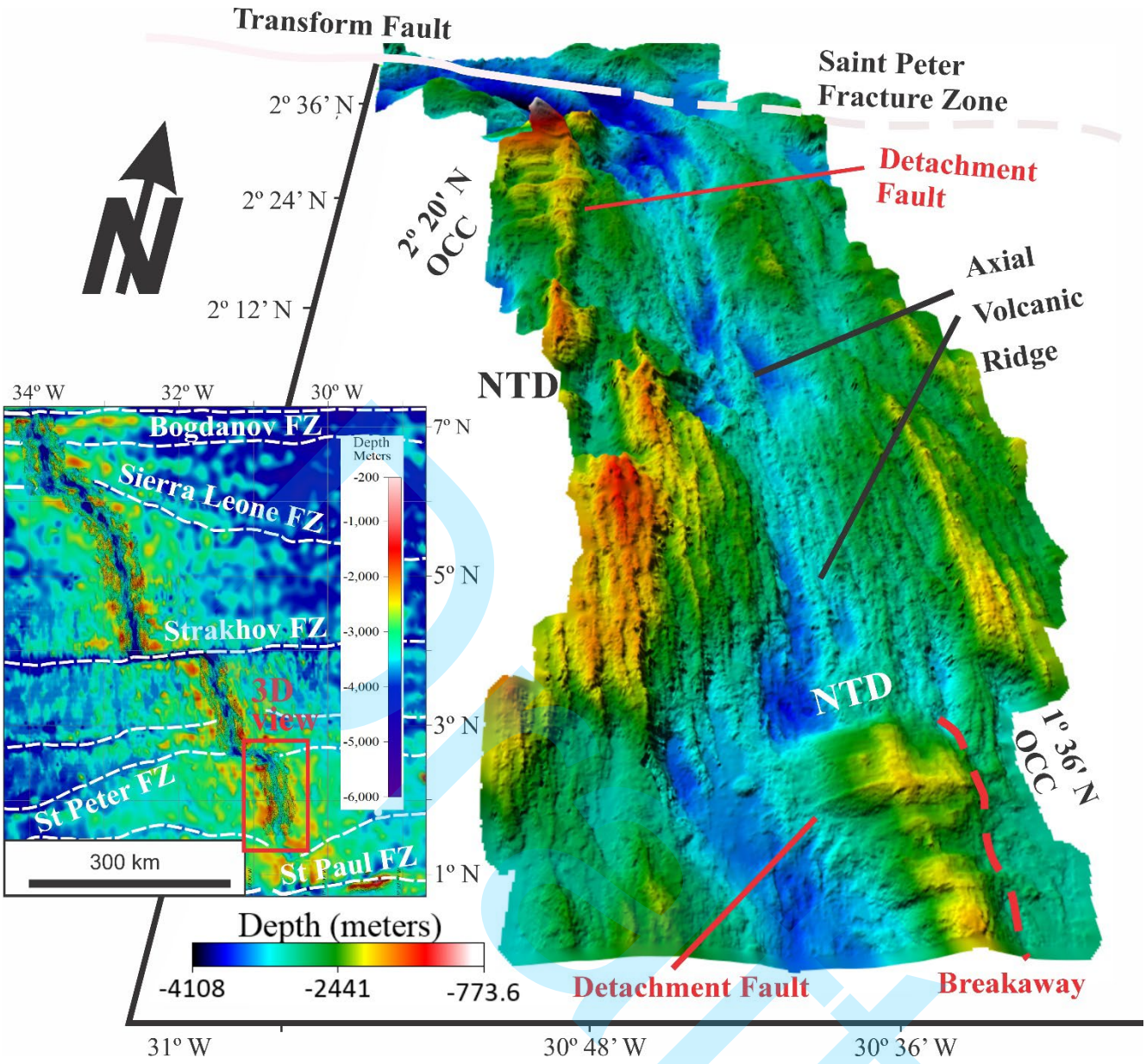

Figure 10 - 3D view of the 2º N Segment with 3 times vertical exaggeration.

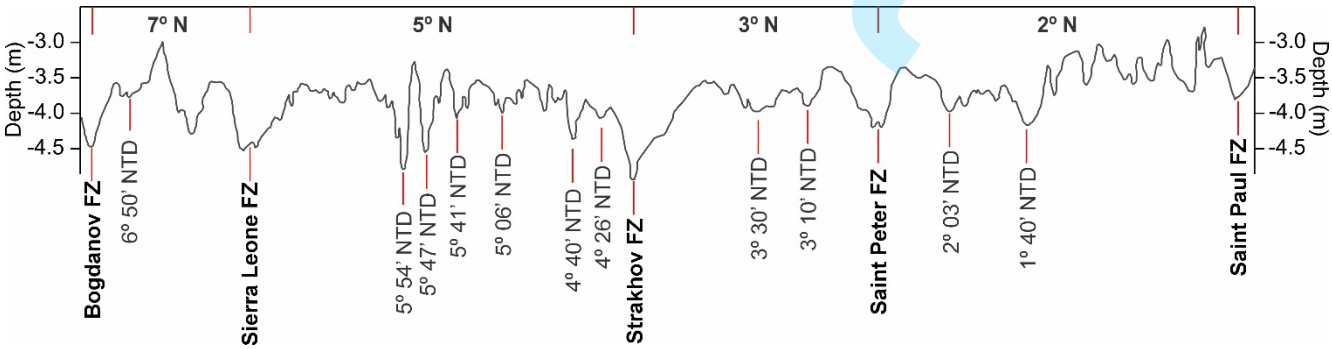

Figure 11 - Bathymetric profile along the axis of the MAR between the Bogdanov (7º 10' N) and St Paul (0º 50' N) fracture zones. Each ridge segment is numbered, see Figure 2.

DISCUSSIONS

The Equatorial MAR displays variable magmatic activity and segmentation patterns, with pronounced AVRs and distributed volcanic features along multiple segments. In the 7º N Segment, the pronounced magmatism, with an AVR exceeds 1,000 m in relief from the bottom in the Bogdanov FZ and persist even within the NTDs, indicating sustained magmatic activity across structural boundaries, with several volcanic cones along the sea-floor of the axial valley (Fig. 4). This was also observed by Skolotnev et al. (2022), confirming that AVRs have a critical role in the south of the Bogdanov FZ. This pattern continues in the 5º N Segment, where AVRs and volcanic cones extend across the entire sea-floor of the axial valley, sometimes assuming the orientation of the NTDs (e.g., 5º 47' - 5º 41' N) (Figs. 6 and 11). In contrast, AVRs in the 3° N and 2° N Segments are narrower and shallower (100 - 200 m), suggesting segment-scale variations in magma supply (Figs. 8 and 10). The AVRs are commonly disrupted or absent near NTDs, further underscoring the structural modulation of magmatic processes.

Twelve Oceanic Core Complexes (OCCs) and associated detachment faults were inferred in the survey area, with a clear asymmetry: nine OCCs on the eastern flank and three on the western flank of the ridge segments (Figs. 2 to 10; Tab. 2). All western flank OCCs are interpreted as active structures, located within the axial valley (Figs. 2 to 10; Tab. 2). In contrast, three OCCs - two on the eastern flank (6° 36' N and 3° 43' N) and one on the western flank (2° 20' N) - are interpreted as inactive, occurring 5 to 15 km away from the axial valley (Figs. 4, 8, 10; Tab. 2). This spatial configuration of NTDs and OCCs, resembles hydrothermal and detachment systems observed elsewhere along the MAR, including the Rainbow hydrothermal field at 36° 15' N (Gràcia et al., 2000) and the OCCs between 13° 14' N and 13° 54' N (Macdonald, 1982), supporting the interpretation that OCCs in this present study represent different stages of the tectono-magmatic cycle. In all instances, the detachment faults are preferentially oblique to the spreading axis, and this orientation is echoed in the alignment of corrugated OCC structures along the flanks of the ridge segments.

Oblique faults in the NW-SE direction are consistently observed across all four mapped dorsal segments of the Equatorial Mid-Atlantic Ridge (7º N, 5º N, 3º N, and 2º N). These features are poorly resolved in global datasets such as GEBCO (Fig. 2) and were largely overlooked in previous studies. However, high-resolution bathymetric data revealed their presence of oblique faults within inner rift valleys, along transform faults, and across sedimentary basins (Figs. 2 to 10). These faults are noticeable even at the rift valley floor and are only absent beneath axial neovolcanic ridges. Their NW-SE orientation plays a fundamental role in segment boundary definition, particularly where displacements exceed 50 km and coincide with NTDs. This structural pattern further reinforces the significance of NW-SE oblique faulting in segmentation of the ridge, detachment fault initiation, and consequently the mantle exhumation, especially among eastern-flank OCCs. Thus, the morphological aspect of the Equatorial MAR is strongly influenced by this oblique fault fabric, closely linked to the NW-SE trend, that generate zones of weakness in the oceanic crust, where they shape and delimit the

segments and generate detachment faults, allowing the exhumation of mantle-derived rocks, and shaping long-lived morpho-tectonic domains along the Equatorial MAR.

CONCLUSIONS

This study presents a comprehensive morpho-structural analysis of the Equatorial Mid-Atlantic Ridge (MAR) between the Bogdanov and Saint Paul Fracture Zones, integrating multi-beam bathymetric data, backscatter intensity, and slope maps. The resulting framework reveals a complex tectono-magmatic landscape shaped by both transform and non-transform processes.

Normal faulting displays significant spatial variability, with amplitudes correlating strongly with tectonic settings. Faults are preferentially concentrated in the symmetrical accreting zones, while are asymmetrical flanks in most of the research areas horst OCCs emplaced via detachment faults. Despite the relative scarcity of transform faults, the AVR exhibits frequent offsets governed predominantly times by NTDs.

Uplifting mantle rocks by OCCs is a prevalent mechanism for accretion in this part of the Equatorial MAR (7º 10’ – 0º 50’ N). This mechanism leads to regional uplift and the emplacement of lower crust and upper mantle rocks. The distribution of OCCs — nine on the east flank versus three on the west — suggests asymmetric magmatic supply and contrasting tectonic histories between flanks. Notably, OCC-bearing regions are generally found on ridge sections characterized by lower-than-average seismicity rates. Therefore, the east flank would have a smaller magmatic input, favoring the asymmetrical accretion of this dorsal region. The geology and morphology of the Equatorial MAR segments are controlled by NTD-related dynamics, between 7º 10’ N and 0º 50’ N. Most displacements in the rift valley are NTD controlled.

Overall, the structural evolution of the Equatorial MAR segment between 1° and 7° N is intricately linked to the NTD dynamics, which reflects variations in magmatic productivity and thermal regime, typically associated with higher occurrences of non-transform displacements. These displacements are often the result of localized strain accumulation due to volcanic activity or the interaction of different ridge segments. These findings underscore the critical role of low melt supply and tectonic segmentation in driving OCC formation and crustal architecture in slow-spreading environments.

ACKNOWLEDGEMENTS

This is a contribution to the project Prospecting and Exploration Project for Polymetallic Sulphides in the Mid-Atlantic Ridge (PROCORDILHEIRA). Funds for this research were provided by Geological Survey of Brazil (SGB). We extend special thanks to the crew of the Ocean Stalwart Research Vessels and the PPGG/UFRN for the academic and scientific infrastructure support. Thanks are due to the Brazilian National Council for Scientific and Technological Development (CNPq) for the fellowships to MPG (302375/2022-8).

REFERENCES

Basile, C., I. Girault, J-L. Paquette, A. Agranier, L. Loncke, A. Heuret, and E. Poetisi, 2020, The Jurassic magmatism of the Demerara Plateau offshore French Guiana as a remnant of the Sierra Leone hotspot during the Atlantic rifting. Scientific Reports 10:7486. DOI: 10.1038/s41598-020-64333-5

Blakely, R. J., 1996, Potential theory in gravity and magnetic applications. Cambridge University Press, 441 pp. DOI: 10.1017/CBO9780511549816

Blackman, D. K., J. P. Canales, and A. Harding, 2009, Geophysical signatures of oceanic core complexes. Geophysical Journal International 178(2): 593-613. DOI: 10.1111/j.1365-246X.2009.04184.x

Bonatti, E., A. Peyve, P. Kepezhinskas, N. Kurentsova, M. Seyler, S. Skolotnev, and G. Udintsev, 1992, Upper mantle heterogeneity below the Mid-Atlantic Ridge 0°-15°N. Journal of Geophysical Research, 97(B4): 4461-4476. DOI: 10.1029/91JB02838

Bonatti, E., 1996, Long-lived oceanic transform boundaries formed above mantle thermal minima. Geology 24(9): 803-806. DOI: 10.1130/0091-7613(1996)024<0803:LLOTBF>2.3.CO;2

Cann, J. R., D. K. Blackman, D. K. Smith, E. McAllister, B. Janssen, S. Mello, and J. Escartín, 1997, Corrugated slip surfaces formed at ridge-transform intersections on the Mid-Atlantic Ridge. Nature 385(6614): 329-332. DOI: 10.1038/385329a0

Cannat, M., D. Sauter, V. Mendel, E. Ruellan, K. Okino, J. Escartín, V. Combier, and M. Baala, 2006, Modes of sea-floor generation at a melt-poor ultraslow-spreading ridge. Geology 34(7): 605-608. DOI: 10.1130/G22486.1

Carbotte, S. M., D. K. Smith, M. Cannat, and E. M. Klein, 2015, Tectonic and magmatic segmentation of the Global Ocean Ridge System a synthesis of observations. Geological Society London Special Publications 420(1): 249-295. DOI: 10.1144/SP420.5

Chen, Y. J., 2003, Influence of the Iceland mantle plume on crustal accretion at the inflated Reykjanes Ridge magma lens and low hydrothermal activity. Journal of Geophysical Research Solid Earth 108(B11): 1-12. DOI: 10.1029/2001JB000816

Dannowski, A., J. P. Morgan, I. Grevemeyer, and C. R. Ranero, 2018, Enhanced Mantle Upwelling/Melting Caused Segment Propagation, Oceanic Core Complex Die Off, and the Death of a Transform Fault The Mid-Atlantic Ridge at 21.5°N. Journal of Geophysical Research: Solid Earth 123(2): 941-956. DOI: 10.1002/2017JB014273

Dick, H. J. B., J. H. Natland, J. C. Alt, W. Bach, D. Bideau, J. S. Gee, S. Haggas, J. G. H. Hertogen, G. Hirth, P. M. Holm, B. Ildefonse, G.J. Iturrino, B. E. John, D. S. Kelley, E. Kikawa, A. Kingdon, P. J. LeRoux, J. Maeda, P. S. Meyer, D. J. Miller, H. R. Naslund, Y-L. Niu, P. T. Robinson, J. Snow, R. A. Stephen, P. W. Trimby, H-U. Worm, and A. Yoshinobu, 2000, A long in situ section of the lower oceanic crust Results of ODP Leg 176 drilling at the Southwest Indian Ridge. Earth and Planetary Science Letters 179: 31-51. DOI: 10.1016/S0012-821X(00)00102-3

Escartín, J., C. Mével, C. J. MacLeod, and A. M. McCaig, 2003, Constraints on deformation conditions and the origin of oceanic detachments The Mid-Atlantic Ridge core complex at 15º 45' N. Geochemistry Geophysics Geosystems 4(8): 1067. DOI: 10.1029/2002GC000472

Escartín, J., C. Mével, S. Petersen, D. Bonnemains, M. Cannat, M. Andreani, N. Augustin, A. Bezos, V. Chavagnac, Y. Choi, M. Godard, K. Haaga, C. Hamelin, B. Ildefonse, J. Jamieson, B. John, T. Leleu, C. J. MacLeod, M. Massot-Campos, P. Nomikou, J. A. Olive, M. Paquet, C. Rommevaux, M. Rothenbeck, A. Steinfuhrer, M. Tominaga, L. Triebe, R. Campos, N. Gracias, and R. Garcia, 2017, Tectonic structure, evolution, and the nature of oceanic core complexes and their detachment fault zones 13°20′N and 13°30′N, Mid Atlantic Ridge. Geochemistry Geophysics Geosystems 18(4): 1451-1482. DOI: 10.1002/2016GC006775

Fujiwara, T., J. Lin, T. Matsumoto, P. B. Kelemen, B. E. Tucholke, and J. F. Casey, 2003, Crustal evolution of the Mid-Atlantic Ridge near the fifteen-twenty fracture zone in the last 5 Ma. Geochemistry Geophysics Geosystems 4(3). DOI: 10.1029/2002GC000364

Gràcia, E., J. L. Charlou, J. Radford-Knöery, and L. M. Parson, 2000, Non-transform offsets along the Mid-Atlantic Ridge south of the Azores 38°N-34°N ultramafic exposures and hosting of hydrothermal vents. Earth and Planetary Science Letters 177: 89-103. DOI: 10.1016/S0012-821X(00)00034-0

GEBCO, 2021, Gridded Bathymetry Data. DOI: 10.5285/c6612cbe-50b3-0cff-e053-6c86abc09f8f

Geosoft Oasis Montaj, 2008, The core software platform for working with large volume gravity and magnetic spatial data. Geosoft Inc Toronto Canada.

Grindlay, N. R., P. J. Fox, and P. R. Vogt, 1992, Morphology and tectonics of the Mid-Atlantic Ridge 25°-27°30′S from Sea Beam and magnetic data. Journal of Geophysical Research 97(B5): 6983-7010. DOI: 10.1029/91JB02981

Hayman, N. W., N. R. Grindlay, M. R. Perfit, P. Mann, S. Leroy, and B. M. de Lépinay, 2011, Oceanic core complex development at the ultraslow spreading Mid-Cayman Spreading Center. Geochemistry Geophysics Geosystems, 12(3): Q0AG02. DOI: 10.1029/2010gc003240

Hey, R., F. Martinez, Á. Höskuldsson, and Á. Benediktsdóttir, 2010, Propagating rift model for the V-shaped ridges south of Iceland. Geochemistry Geophysics Geosystems, 11(3). DOI: 10.1029/2009GC002865

Karson, J. A., and P. A. Rona, 1990, Block-tilting transfer faults and structural control of hydrothermal processes in the TAG area Mid-Atlantic Ridge 26°N. Geological Society of America Bulletin, 102(12): 1635-1645. DOI: 10.1130/0016-7606(1990)102<1635:BTTFAS>2.3.CO;2

Kilsdonk, B., J. Trude, T. Grow, B. Ott, and G. Manatschal, 2024, Complete transition from mantle plume to mantle exhumation on the Central Atlantic Guyana/Suriname margin. Communications Earth Environment 5: 112. DOI: 10.1038/s43247-024-01265-2

Le Voyer, M., E. Cottrell, K. A. Kelley, M. Brounce, and E. H. Hauri, 2015, The effect of primary versus secondary processes on the volatile content of MORB glasses: An example from the Equatorial Mid-Atlantic Ridge 5°N-3°S. Journal of Geophysical Research: Solid Earth 120(1): 125-144. DOI: 10.1002/2014JB011160

Macdonald, K. C., 1982, Mid-ocean ridges: fine scale tectonic volcanic and hydrothermal processes within the plate boundary zone. Annual Review of Earth and Planetary Sciences 10: 155-190. DOI: 10.1146/annurev.ea.10.050182.001103

MacLeod, C. J., R. C. Searle, B. J. Murton, J. F. Casey, C. Mallows, S. C. Unsworth, K. L. Achenbach, and M. Harris, 2009, Life cycle of oceanic core complexes. Earth and Planetary Science Letters 287(34): 333-344. DOI: 10.1016/j.epsl.2009.08.016

Maia, M., S. Sichel, A. Briais, D. Brunelli, M. Ligi, N. Ferreira, T. Campos, B. Mougel, I. Brehme, C. Hémond, A. Motoki, D. Moura, C. Scalabrin, I. Pessanha, E. Alves, A. Ayres, and P. Oliveira, 2016, Extreme mantle uplift and exhumation along a transpressive transform fault. Nature Geoscience 9(8): 619-623. DOI: 10.1038/ngeo2759

Mckenzie, D., and M. J. Bickle, 1988, The volume and composition of melt generated by extension of the lithosphere. Journal of Petrology 29(3): 625-679. DOI: 10.1093/petrology/29.3.625

Mazarovich, A. O., S. Y. Sokolov, N. N. Turko, and K. O. Dobrolyubova, 2001, Sea-floor topography and structure of the rift zone of the Mid-Atlantic Ridge between 5° and 7°18'N. Russian Journal of Earth Sciences 3(5): 353-370. DOI: 10.2205/2001ES000071

Peirce, C., G. Reveley, A. H. Robinson, M. J. Funnell, R. C. Searle, N. M. Simão, C. J. MacLeod, and T. J. Reston, 2019, Constraints on crustal structure of adjacent OCCs and segment boundaries at 13°N on the Mid-Atlantic Ridge. Geophysical Journal International 217(2): 988-1010. DOI: 10.1093/gji/ggz074

Petersen, S., K. Kuhn, T. Kuhn, N. Augustin, R. Hékinian, L. Franz, and C. Borowski, 2009, The geological setting of the ultramafic-hosted Logatchev hydrothermal field (14°45′N, Mid-Atlantic Ridge) and its influence on massive sulfide formation. Lithos 112(1–2): 40-56. DOI: 10.1016/j.lithos.2009.02.008

Reston, T. J., and C. R. Ranero, 2011, The 3-D geometry of detachment faulting at mid-ocean ridges. Geochemistry Geophysics Geosystems 12(7): 1-19. DOI: 10.1029/2011GC003666

Rosencrantz, E., M. I. Ross, and J. G. Sclater, 1988, Age and spreading history of the Cayman Trough as determined from depth, heat flow, and magnetic anomalies. Journal of Geophysical Research: Solid Earth 93(B3): 2141-2157. DOI: 10.1029/JB093iB03p02141

Sandwell, D. T., R. D. Müller, W. H. F. Smith, E. Garcia, and R. Francis, 2014, New global marine gravity model from CryoSat-2 and Jason-1 reveals buried tectonic structure. Science, 346(6205): 65-67. DOI: 10.1126/science.1258213

Savel'eva, G. N., N. S. Bortnikov, A. A. Peyve, and S. G. Skolotnev, 2006, Ultramafic rocks from the Markov Deep in the rift valley of the Mid-Atlantic Ridge. Geochemistry International 44(11): 1105-1120. DOI: 10.1134/S0016702906110024

Savel'eva, G. N., N. S. Bortnikov, T. B. Bayanova, S. V. Ikorskii, and I. L. Kamenskii, 2008, Sm-Nd and Rb-Sr isotopic systems and captured He and hydrocarbon gases as markers of melt sources and fluid regime under which the oceanic crust of the Mid-Atlantic Ridge was formed at 5°-6°N. Geochemistry International 46(8): 745-758. DOI: 10.1134/S0016702908080016

Sani, C., A. Sanfilippo, S. Skolotnev, M. Ligi, F. Genske, and A. Stracke, 2024, Sampling Earth's mantle at intra-transform spreading ridges. Geochimica et Cosmochimica Acta 374: 156-172. DOI: 10.1016/j.gca.2024.04.032

Schilling, J., B. B. Hanan, B. Mccully, R. H. Kingsley, and D. Fontignie, 1994, Influence of the Sierra Leone mantle plume on the Equatorial Mid-Atlantic Ridge A Nd-Sr-Pb isotopic study. Journal of Geophysical Research: Solid Earth 99(B6): 12005-12028. DOI: 10.1029/94JB00337

Schilling, J. G., C. Ruppel, A. N. Davis, B. McCully, S. A. Tghe, R. H. Kingsley, and J. Lin, 1995, Thermal structure of the mantle beneath the Equatorial Mid-Atlantic Ridge Inference from the spatial variation of dredged basalt glass compositions. Journal of Geophysical Research: Solid Earth 100(B6): 10057-10076. DOI: 10.1029/95JB00668

Schroeder, T., and B. E. John, 2004, Strain localization on an oceanic detachment fault system Atlantis Massif, 30ºN, Mid-Atlantic Ridge. Geochemistry Geophysics Geosystems 5(11): Q11007. DOI: 10.1029/2004GC000728

Sempéré, J-C., J. Lin, H. S. Brown, H. Schouten, and G. M. Purdy, 1993, Segmentation and morphotectonic variations along a slow-spreading center The Mid-Atlantic Ridge 24°00′N-30°40′N. Marine Geophysical Research 15: 153-200. DOI: 10.1007/BF01204232

Simpson, R. W., R. C. Jachens, and R. J. Blakely, 1983, AIRYROOT: a Fortran program for calculating the gravitational attraction of an Airy isostatic root out to 166.7 km. Open-File Report 83-883. DOI: 10.3133/ofr83883

Smith, W. H. F., and P. Wessel, 1990, Gri-ding with continuous curvature splines in tension. Geophysics 55(3): 293-305. DOI: 10.1190/1.1442837

Smith, D. K., J. Escartín, H. Schouten, and J. R. Cann, 2008, Fault rotation and core complex formation Significant processes in sea-floor formation at slow-spreading mid-ocean ridges (Mid-Atlantic Ridge, 13°-15°N). Geochemistry Geophysics Geosystems 9(3) DOI: 10.1029/2007GC001699

Smith, D. K., H. Schouten, H. J. B. Dick, J. R. Cann, V. Salters, H. R. Marschall, F. Ji, D. Yoerger, A. Sanfilippo, R. Parnell-Turner, C. Palmiotto, A. Zheleznov, H. Bai, W. Junkin, B. Urann, S. Dick, M. Sulanowska, P. Lemmond, and S. Curry, 2014, Development and evolution of detachment faulting along 50 km of the Mid-Atlantic Ridge near 16.5°N. Geochemistry Geophysics Geosystems 15(12): 4692-4711. DOI: 10.1002/2014GC005563

Skolotnev, S. G., A. A. Peyve, S. M. Lyapunov, V. A. Simonov, Y. E. Glazyrin, and V. Y. Kolobov, 2003, MAR volcanism in the Sierra Leone fracture Zone region, Central Atlantic. Russian Journal of Earth Sciences 5(2): 101-123. DOI: 10.2205/2003ES000117

Skolotnev, S. G., A. Sanfilippo, A. A. Peyve, F. Muccini, S. Y. Sokolov, C. Sani, K. O., Dobroliubova, C., Ferrando, N. P., Chamov, C., Palmiotto, A. N., Pertsev, E., Bonatti, M., Cuffaro, A. C., Gryaznova, K. N., Sholukhov, A. S., Bich, and M. Ligi, 2019, Large-scale structure of the Doldrums multi-fault transform system (7-8ºN Equatorial Atlantic): preliminary results from the 45th expedition of the R/V A.N. Strakhov. Ofioliti 45(1): 25-41. DOI: 10.4454/ofioliti.v45i1.553

Skolotnev, S. G., K. O. Dobrolyubova, A. A. Peyve, S. Y. Sokolov, N. P. Chamov, and M. Ligi, 2022, Structure of Spreading Segments of the Mid-Atlantic Ridge between the Arkhangelsky and Bogdanov Transform Faults, Equatorial Atlantic. Geotectonics 56(1): 1-20. DOI: 10.1134/S0016852122010083

Skolotnev, S. G., K. O. Dobrolyubova, A. A. Peyve, S. Y. Sokolov, N. P. Chamov, and M. Ligi, 2023, Fracture Zones of the Doldrums Megatransform System Equatorial Atlantic. Geotectonics 57(4): 361-385. DOI: 10.1134/S0016852123040118

Sokolov, S. Y., Y. A. Zaraiskaya, A. O. Mazarovich, V. N. Efimov, and N. S. Sokolov, 2016, Spatial instability of the rift in the St. Paul multifault transform fracture system, Atlantic Ocean. Geotectonics 50(3): 223-237. DOI: 10.1134/S0016852116030110

Tucholke, B. E., J. Lin, M. C. Kleinrock, M. A. Tivey, T. B. Reed, J. A. Goff, and G. E. Jaroslow, 1997, Segmentation and crustal structure of the western Mid-Atlantic Ridge flank, 25º25'-27º10'N and 0-29 m.y. Journal of Geophysical Research: Solid Earth 102 (B5): 10203-10223. DOI: 10.1029/96JB03896

Tucholke, B. E., J. Lin, and M. C. Kleinrock, 1998, Megamullions and mullion structure defining oceanic metamorphic complexes on the Mid-Atlantic Ridge. Journal of Geophysical Research: Solid Earth 103(B5): 9857-9866. https://doi.org/10.1029/98JB00167

Tucholke, B. E., M. D. Behn, W. R. Buck, and J. Lin, 2008, Role of melt supply in oceanic detachment faulting and formation of megamullions. Geology 36(6): 455-458. https://doi.org/10.1130/G24639A.1

Udintsev, G.B., 1996, Equatorial Segment of the Mid-Atlantic Ridge Initial Results of the Geological and Geophysical Investigations under the EQUARIDGE Program Cruises of R/V 'Akademik Nikolaj Strakhov' in 1987, 1990, 1991. IOC Technical series 46 UNESCO Paris.

United States Geological Survey, 2021, Earthquakes. Retrieved October 12, 2021, from Earthquakes website. https://earthquake.usgs.gov/earthquakes/map/

Whitney, D. L., C. Teyssier, P. Rey, and W. R. Buck, 2013, Continental and oceanic core complexes. Bulletin of the Geological Society of America 125(3-4): 273-298. DOI: 10.1130/B30754.1

Zheng, T., B. E. Tucholke, and J. Lin, 2019, Long-Term Evolution of Nontransform Discontinuities at the Mid-Atlantic Ridge, 24°N-27°30′N. Journal of Geophysical Research Solid Earth 124(10): 10023-10055. DOI: 10.1029/2019JB017648.

Simões, H. A.: conceptualization, data curation, investigation, methodology, resources, visualization, writing – original draft; **Gomes, M. P.:** formal analysis, methodology, supervision, visualization, writing – original draft, writing – review & editing; **Oliveira, P. R. A.:** formal analysis, investigation, methodology, resources, visualization, writing – review & editing; **Souza, M. L.:** investigation, writing – review & editing; **Rocha, H. L. A.:** formal analysis, investigation, methodology, visualization, writing – review & editing; **Harlamov, V.:** conceptualization, data curation, funding acquisition, resources, writing – review & editing.